


Article

Shape Dependence of Photoresponsive Molecular Crystals Composed of Naphthyl Acrylic Acid Stimulated by Solid-State [2 + 2] Photocycloaddition

Tian-Yuan Li, Yu-Ze Du, Tian-Yi Xu, Tian-Le Zhang and Fei Tong * 

Key Laboratory for Advanced Materials and Joint International Research Laboratory of Precision Chemistry and Molecular Engineering, Feringa Nobel Prize Scientist Joint Research Center, Frontiers Science Center for Materiobiology and Dynamic Chemistry, School of Chemistry and Molecular Engineering East China University of Science and Technology, 130 Meilong Road, Shanghai 200237, China; lnyvengo@163.com (T.-Y.L.); 15693555915@163.com (Y.-Z.D.); xutianyi1108@163.com (T.-Y.X.); y20190127@mail.ecust.edu.cn (T.-L.Z.)

* Correspondence: feitong@ecust.edu.cn

Abstract: Photomechanical molecular crystals, actuated by solid-state photochemical reactions, manifest a spectrum of mechanical motions upon light exposure, underscoring their prospective integration into the next generation of intelligent materials and devices. Utilizing the solid-state photodimerization of naphthyl acrylic acid as a paradigm, this study delved into the interplay between crystal morphology and reaction dynamics on the photomechanical responses of molecular crystals. Distinct crystal forms—bulk, microrods, and microplates—were cultivated through tailored crystallization conditions. While bulk crystals of naphthyl acrylic acid (NA) underwent shattering and splintering upon UV light exposure, the microplate counterparts displayed unique cracking patterns with fissures yet retained their overall structural integrity. In contrast, NA microrods underwent pronounced bending under identical irradiation conditions. These phenomena are attributed to the efficient lattice reconfiguration stemming from the [2 + 2] cycloaddition photochemical reaction within the crystals. An intermediate fluorescence enhancement was observed across all crystal types upon light exposure. Collectively, our results underscore the pivotal role of crystal shape in dictating photomechanical behavior, thereby heralding novel strategies for developing advanced photomechanical materials.



Citation: Li, T.-Y.; Du, Y.-Z.; Xu, T.-Y.; Zhang, T.-L.; Tong, F. Shape Dependence of Photoresponsive Molecular Crystals Composed of Naphthyl Acrylic Acid Stimulated by Solid-State [2 + 2] Photocycloaddition.

Crystals **2024**, *14*, 492. <https://doi.org/10.3390/cryst14060492>

Received: 25 April 2024

Revised: 17 May 2024

Accepted: 19 May 2024

Published: 23 May 2024



Copyright: © 2024 by the authors. Licensee MDPI, Basel, Switzerland. This article is an open access article distributed under the terms and conditions of the Creative Commons Attribution (CC BY) license (<https://creativecommons.org/licenses/by/4.0/>).

Keywords: fluorescence; crystal growth; crystal engineering; photochemistry; [2 + 2] cycloaddition

1. Introduction

Solid-state photoresponsive materials exhibiting mechanical motions or shape deformations driven by various photochemical reactions have recently attracted increasing interest [1–4]. The versatile mechanically responsive behaviors involving bending [5–10], twisting [11–15], curling [16–19], and expanding [20–23] can be potentially applied in photoactuators, soft robots, photoswitches, optical information storage, and artificial muscles via regulating the excitation light [24]. Unlike photoresponsive polymers, molecular crystals directly consisting of photoactive molecules can also display robust photomechanical responses when exposed to light [25–31]. Except for relatively high densities and elastic modulus, structural transformations and geometric changes at the molecular level can be effectively transduced and collectively amplified to the multiple scales in a molecular crystal, generating macroscopic motions, such as jumping and splintering. Moreover, obtaining both single crystal structures of reactant and photoproduct through X-ray diffraction characterization and investigating intermediate processes is also possible.

However, detailed investigation and analysis of these vigorous mechanical motions are still challenging. This is because a crystal may suffer from disintegration or shattering because of the intense internal strains generated during a photochemical reaction. Recent

research has suggested that crystal shape and morphology play essential roles in determining crystal photomechanical habits, and smaller crystals can remain intact even after dramatic deformations [32]. For instance, Bardeen et al. showed that the different microcrystals of 9-methylanthracene with varying ratios of aspect of width and length would result in bending or twisting motion upon the same excitation light irradiation [14,33–35]. Diarylethene crystals of the same molecule exhibit disparate photoresponses in bulk and crystal nanowires.

Inspired by this, we present here the vivid photoresponses in molecular crystals composed of the photoactive (*E*)-3-(naphthalen-2-yl) acrylic acid (NA) molecules. Our research unveils that the photomechanical motions of these crystals exhibit shape-dependence properties when exposed to ultraviolet (UV) light (Figure 1a). Unlike the shattering and splintering observed in the NA bulk crystals, the NA microcrystal plates show distinctive cracking with fissures while maintaining their overall morphology after UV light irradiation. Conversely, the NA microcrystal rods exhibit significant bending under the same light irradiation. These diverse photomechanical responses are all initiated by the same head-to-head [2 + 2] photocycloaddition of NA molecules in crystals, leading to significant molecular structure changes that enable macroscopic motions. Moreover, we observed intermediate fluorescence enhancement in all crystals during the light illumination, indicating that molecular configuration and crystal packing changes may facilitate radiation transition during photochemistry. The computational calculations also reveal that the excited monomer and photo-generated dimer molecules can establish robust intermolecular interactions, allowing for the intermediate state to emit fluorescence temporally. Lastly, we demonstrated the fabrication of a simple turning on/off information storage system based on the intriguing feature of the NA crystals. Our results showed a straightforward strategy to achieve versatile photoresponses in dynamic molecular crystals, hinting at their potential in information storage.

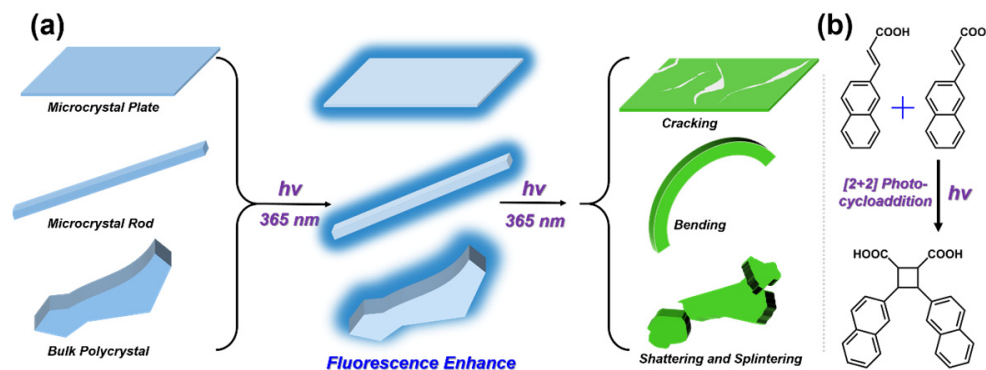


Figure 1. (a) NA crystals with different morphologies and shapes exhibiting different photoresponsive behaviors under UV light (365 nm) irradiation. During the light irradiation, crystals displayed enhanced fluorescence emission compared to the reactants and photoproducts. (b) The robust photomechanical responses were stimulated by a head-to-head [2 + 2] photocycloaddition.

2. Materials and Methods

All the chemicals and reagents for synthetic purposes used in this work were purchased from TCI, Adamas-beta, and Sigma-Aldrich, being used without further purification. Milli-Q water (18 M Ω /cm) was used throughout the experiments. Filter papers that were used for pattern transferring and erasing were purchased from Titan Scientific Co., Ltd. (Shanghai, China). The ^1H and ^{13}C NMR spectra were measured on a Bruker AV-600 (Fällanden, Switzerland) spectrometer at 298 K. The LCT Premier XE mass spectrometer was from the Waters Company of the United States (Milford, MA, USA). The UV–VIS absorption spectra data were documented by a Shimadzu UV-2600 UV–VIS spectrophotometer (Kyoto, Japan, Shimadzu), and the fluorescence spectra were acquired by a Shimadzu RF6000 spectrofluorophotometer (Japan, Shimadzu). The optical microscopy measure-

ments were conducted using a Leica DM750 microscope equipped with a QTF500 digital camera (Wetzlar, Germany). The microscopy fluorescence measurements were performed using a TL-3201LED fluorescence microscope (equipped with a 20MP USB 3.0 digital camera, Shanghai, China). All PXRD data were collected on an X-ray powder diffractometer (Rigaku, Tokyo, Japan 18 kW/D/Max2550VB/PC, CuK α radiation, $\lambda = 1.5418 \text{ \AA}$, 40 kV/100 mA power) at room temperature (divergence slit = 1.00 mm without monochromator). The scanning electron microscopy (SEM) analyses were presented with a Helios G4 UC. The photoluminescence quantum yield was measured on Quantaury-QY Plus from Hamamatsu (Japan). The ground state geometries of NA were optimized by density functional theory (DFT) at the B3LYP/6-31G level in Gaussian 09W software (Revision E.01). The non-covalent interaction index (NCI) analysis was undertaken by the Multiwfn program and visualized using the (multiwfn 3.6) VMD software package.

2.1. ^1H NMR Measurements

In the synthesis of compounds, 5 mg of the NA solid powder was dissolved in 0.5 mL of acetone- d_6 . For the preparation of liquid samples, approximately 5 mg of the solid powder was initially dissolved in a deuterated solvent, such as deuterated dimethyl sulfoxide (DMSO- d_6), to achieve a homogeneous solution. Subsequently, these solutions were subjected to varying durations of light exposure prior to undergoing NMR analysis. In the case of solid samples, approximately 5 mg of microcrystals were directly irradiated with 365 nm light for specified intervals, followed by dissolution in a deuterated solvent to prepare a solution for NMR analysis. To prevent exposure to ambient light during shipment, all NMR sample tubes were shielded with aluminum foil.

2.2. Optical Microscopy Measurements

A suspension containing an NA microplate or microrod crystals was applied as a single drop onto a glass microscope slide and secured with a coverslip. The photomechanical behavior of the NA microcrystals was observed using a Leica DM750 microscope, which was integrated with a QTF500 digital camera. The specimens were exposed to visible light emitted by the microscope, with an average irradiance of approximately 5 mW/cm^2 . For fluorescence microscopy assessments, an Olympus IX73 inverted research microscope, fitted with a CoolSnap HQ2 digital camera (Shanghai, China), and a TL-3201LED fluorescence microscope (Shanghai, China), equipped with a 20-megapixel USB3.0 digital camera (Shanghai, China), were utilized.

2.3. Optical Spectroscopy Measurements

For the solution-phase samples, 2 mL of the NA solution in tetrahydrofuran (THF) was transferred into a cuvette. The sample underwent irradiation with 365 nm light for varying durations, following which the UV-VIS absorption spectra were recorded. In the case of photoreacted solid-state samples, 2 mg of NA crystals were irradiated with visible light for distinct intervals before being dissolved in THF to create a diluted solution for UV-VIS absorption spectroscopic analysis. The UV-VIS absorption spectra were measured using a Shimadzu UV-3600 Plus spectrophotometer, which was operated at a high scanning rate.

For the preparation of solid-state samples, a polycrystalline thin film of NA was fabricated via a standard drop-casting technique. Specifically, a quantity of NA solid powder (25–35 mg) was dissolved in 500 μL of THF to achieve a homogeneous solution. This solution was then applied to a flat quartz substrate (1 cm \times 5 cm), and the substrate was stored in darkness for 4 h to facilitate the evaporation of THF. Subsequently, the sample was irradiated with 365 nm light for various time periods, after which the fluorescence spectra were captured.

All steps of the sample preparation, with the exception of the irradiation process, were conducted in a darkroom. Furthermore, to prevent exposure to ambient light, light-tight containers were employed for the transportation and storage of the samples.

2.4. Scanning Electron Microscopy (SEM) Measurements

A small volume of NA microcrystal suspension was applied onto a pristine anodic aluminum oxide (AAO) template featuring a nominal pore diameter of approximately 200 nm (manufactured by Top Membranes Technology Co., Ltd., Shenzhen, China) with an inorganic filter membrane diameter of 12.5 mm and a nominal pore size of approximately 0.2 μm . Subsequently, excess deionized water was employed to wash away any residual solution. The AAO-templated crystals were subsequently air-dried in a dark chamber at a temperature of 30 °C for a period of 24 h prior to scanning electron microscopy (SEM) analysis. The AAO template, with the adhered crystals, was affixed to a piece of carbon tape, which was then mounted onto an SEM stub. Similarly, the bulk NA crystals were attached directly to a separate piece of carbon tape and secured to an SEM stub. The stub was subsequently introduced into a low-vacuum sputter coater (Leica EM ACE200, Wetzlar, Germany) and sputter-coated with a thin layer of gold for 120 s to achieve a thickness of approximately 5 nm, thereby enhancing the electrical conductivity of the samples. The SEM examination was performed using a Helios G4 UC microscope, employing a 2 kV electron beam in conjunction with an Everhart–Thornley secondary electron detector (ETD) and an Elstar in-lens secondary electron/backscattered electron detector (TLD-SE) (Thermo Fisher Scientific, Hillsboro, OR, USA).

2.5. PXRD Measurements

Aliquots of the NA microcrystal suspension, containing both plate- and rod-shaped morphologies, were carefully deposited onto a pristine anodic aluminum oxide (AAO) template. The template was then thoroughly rinsed with copious amounts of Milli-Q purified water to eliminate any residual solvent, followed by drying through vacuum filtration. Subsequently, the AAO-templated crystals were air-dried in a dark chamber at a temperature of 30 °C for a duration of 24 h prior to analysis.

The collection of all powder X-ray diffraction (PXRD) data was performed using an X-ray diffractometer (model Rigaku D/Max2550VB/PC (Japan), equipped with Cu $K\alpha$ radiation source, $\lambda = 1.5418 \text{ \AA}$, operated at 40 kV and 100 mA) at ambient temperature. The measurements were conducted utilizing the Bragg–Brentano parafocusing geometry. The sample holder was secured in a horizontal position, while the detector, featuring a divergence slit of 1.00 mm and operating without a monochromator, was rotated around the stationary sample in steps of 0.02°.

2.6. Bulk Crystal Preparation

White, bulk-like single crystals of NA were obtained through vapor diffusion under ultrapure aqueous vapors in THF. A small amount (almost 10 mg) of powder from NA was dissolved in tetrahydrofuran to create a homogeneous, saturated solution in two separate glass vials. The vials were then opened and left in the dark under an atmosphere of ultrapure water vapor for three days to allow for solvent evaporation. Large-scale single crystals were grown and used for single crystal analysis and photomechanical response observation after complete evaporation of the solvent from the vials.

2.7. Microrod Crystal Preparation

The NA microrod crystals were prepared using the floating drop method. A solution of 8.5 mg of NA powder in 1.0 mL of filtered ethyl acetate (Adamas-beta, Shanghai, China $\geq 99.0\%$) was gently added to the surface of purified water (MilliQ Millipore) in a Petri dish (Titan, Shanghai, China, 60 \times 15 mm). The Petri dish was covered and left in the dark for 48 h. During this period, the solvent gradually evaporated, resulting in the slow crystallization of NA into microrod that floated on the water surface.

2.8. Microplate Crystal Preparation

The NA microplate crystals were prepared using the surfactant-mediated growth method. We dissolved NA solid in N,N-dimethylformamide (DMF) to obtain a homoge-

neous solution with a concentration of 0.25 M. We prepared an aqueous solution of 0.025 M sodium dodecyl sulfate (SDS). We took 10 mL of the SDS solution in a 20 mL vial and immersed it in a water bath maintained at 55 °C. We then allowed the SDS solution to reach a stable temperature of 55 °C before quickly injecting 100 µL of the NA sample solution. We rapidly injected 50 µL of the NA sample solution into 10 mL of the stabilized 0.02 M SDS solution at 55 °C. We then mixed the solution thoroughly by rapid shaking. Subsequently, we injected 25 µL of the NA crystal seeds solution obtained from a previous precipitation step. Finally, we placed the mixed solution in an oven at 55 °C and incubated it for 3 h in the dark to obtain microplate crystals.

2.9. Computational Methods

The molecular geometries of all monomers and dimers under investigation were optimized comprehensively using density functional theory (DFT) calculations at the B3LYP/6-31G computational level. To confirm that each optimized structure represents a genuine minimum on the potential energy surface, frequency calculations were executed at the identical theoretical level. These computational analyses were conducted utilizing the Gaussian 09 software suite. Subsequently, the non-covalent interaction index (NCI) analysis was performed using the Multiwfn program, with the resulting data visualized employing the Visual Molecular Dynamics (VMD) software package.

3. Results and Discussion

The NA compound features a naphthalene backbone and an acrylic group at the tail. More detailed synthetic information can be found in the Supporting Information (Figures S1–S4). The UV–VIS absorption spectrum of an NA solution sample (tetrahydrofuran (THF) as a solvent, $[NA] = 1.4 \times 10^{-5}$ M) displayed four peaks at 260 nm, 268 nm, 297 nm, and 308 nm, corresponding to $\pi \rightarrow \pi^*$ transitions of the NA molecule (Figure 2a). Compared to the absorption spectrum of naphthalene, the absorption peaks were red-shifted by approximately 20 nm in the NA due to enhanced electronic conjugation by the vinyl structure and electron-withdrawing effect of the carboxylic acid group [35]. The spectra of the solution exhibited a decreasing trend when exposed to UV light (305 nm, 20 mW/cm²). The spectrum remained unchanged after 15 min light irradiation, indicating that the solution might reach a photostationary state. However, as we did not observe any isosbestic point in the spectra, the underlying photochemical reaction in the solution may not be ascribed to a sole *E*-to-*Z* photoisomerization. Proton nuclear magnetic resonance (¹H NMR) measurements of a solution sample with a higher concentration ($[NA] = (5.0 \times 10^{-2}$ M)) exhibited that the photoproducts contained both photodimer and *Z*-isomer molecules due to the [2 + 2] photocycloaddition and *E*-to-*Z* photoisomerization, respectively (Figure 2b). When irradiation time was around 5 min, the chemical shifts associated with the hydrogen atoms in a cyclobutane structure resulting from a photocycloaddition appeared at around 3.9 and 4.4 ppm. Meanwhile, the chemical shift associated with the hydrogen atom in the *Z*-isomer due to the photoisomerization appeared at around 5.7 ppm (Figure 2b, yellow-green trace). The generated photodimer gradually increased as the duration of light irradiation extended. The photodimer was able to reach around 86% when the irradiation time was extended to 90 min, where no *Z*-isomer was observed (Figure 2b, purple trace). We deduced that photoisomerization and photocycloaddition could simultaneously occur, leading to a photostationary state in a dilute solution under light irradiation. The formation of photodimer molecules was also verified by high-resolution mass spectroscopy characterization (Figure S5).

Moreover, because the concentration of a solution sample for the NMR measurements was more than two orders of magnitudes higher, the photoisomerization was likely suppressed by the photocycloaddition with the prolonged irradiation time. The UV–VIS absorption spectrum of a solid NA sample demonstrated narrow absorbance, extending from 210 to 400 nm (Figure S6). Nevertheless, the bulk NA crystals displayed robust photoresponses, characterized by fragmentation and hopping, upon exposure to light. To

achieve consistent and stable optical absorption measurements, we alternatively prepared dilute solutions by dissolving photoreacted solids that had been subjected to varying durations of irradiation in tetrahydrofuran (THF), ensuring equal concentrations across the samples prior to measuring the absorption spectra (Figure 2c). As for the NMR measurements, we obtained solid-state photoproduct mixtures containing both NA monomer and photodimer molecules after light irradiation. We then dissolved the photoproduct mixtures in a deuterated solvent (acetone- d_6) and measured the ^1H NMR for the resulting photoproduct (Figure 2d). The two newly appeared doublets at 4.4 ppm and 3.9 ppm are thought to correspond to the hydrogen atoms in the cyclobutane ring of the photodimer molecule. We only found that $[2 + 2]$ photocycloaddition proceeded in the NA solid samples (Figure 2c,d). The photochemical reaction rate was faster than that of liquid solutions, and photochemistry progressed to almost completion when the irradiation period was 90 min (Figure 2d, purple traces). Photodimers obtained by post-UV irradiation were exposed to light with different wavelengths for one hour, and the reversibility was monitored via the NMR measurements. Our findings indicated that there was an absence of hydrogen proton peak signals corresponding to the monomers under irradiation conditions of 405 nm, 450 nm, and 535 nm, suggesting that the $[2 + 2]$ photodimerization was not reversible in the solid state (Figure S7). According to the thermal gravimetric analysis (TGA) and differential scanning calorimetry (DSC) measurements, both NA and photodimers were thermally stable (Figures S8 and S9).

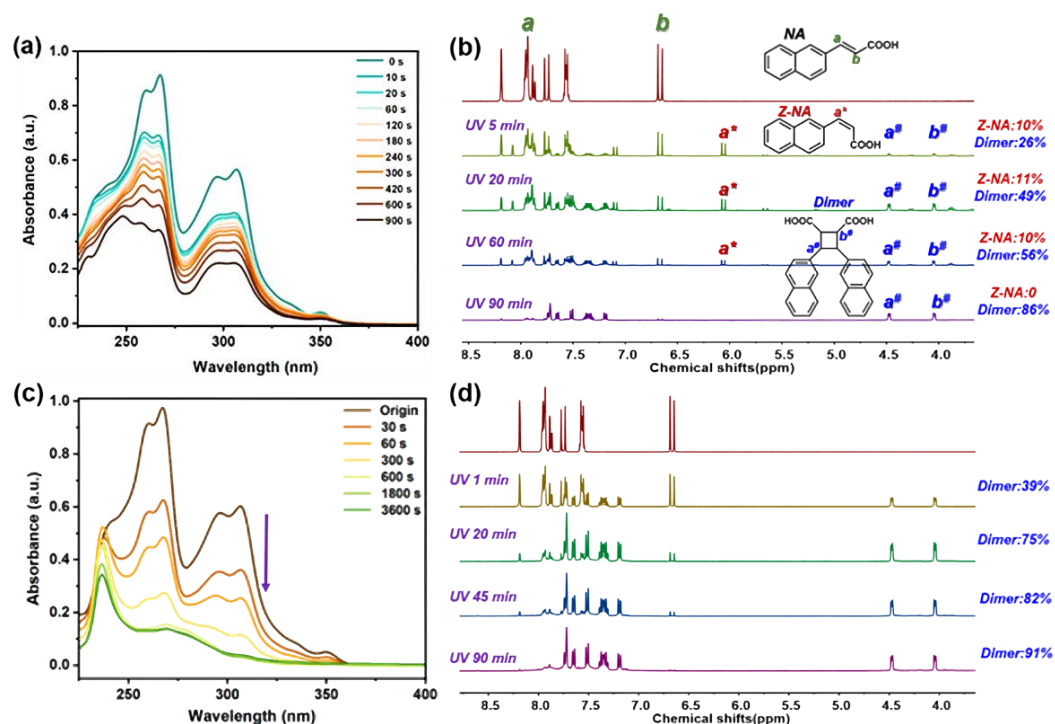


Figure 2. (a) UV–VIS absorption spectra of the NA in tetrahydrofuran (THF) under UV light irradiation. (b) ^1H NMR spectra of the NA in the deuterated dimethyl sulfoxide (DMSO- d_6) under UV light irradiation. (c) UV–VIS absorption spectra of the illuminated solid samples with different light exposure periods dissolved in the THF. (d) ^1H NMR spectra of the illuminated solid samples with different light exposure periods dissolved in the DMSO- d_6 .

High-quality single crystals of NA were obtained using a slow solvent evaporation method. The single crystal structure of the NA molecules also indicates that photocycloaddition was favored in the solid state. As shown in Figure 3a, the NA molecules showed a lamellar stacking structure and adopted a head-to-head packing motif belonging to the $\text{P}\bar{1}$ space group (Table S1). The intermolecular distance of paired NA monomeric molecules was approximately 3.917 Å, allowing an effective $[2 + 2]$ photocycloaddition according

to the Schmidt topological principle on solid-state photochemistry [36]. The intermolecular length exceeded the longest π - π intermolecular distance (3.5 Å), allowing effective fluorescence emission. As a result, solid-state NA powders exhibited a broad fluorescence emission band at around 400–500 nm with a photoluminescence quantum yield (PLQY) of around 0.067 (Figure S10).

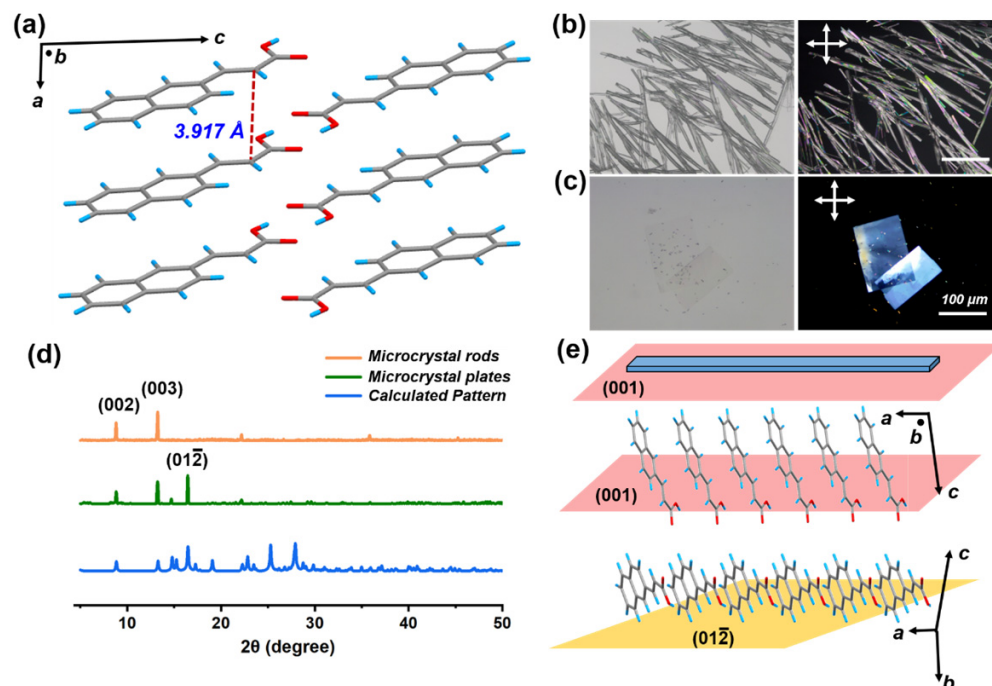


Figure 3. (a) Single crystal structure of the NA viewed along the crystallographic *b*-axis. (b,c) Optical and cross-polarized microscope images of NA microcrystal rods and plates. (d) PXRD patterns of calculated NA, microcrystal plates, and rods. (e) Cartoons showing molecular orientations along the (001) and (012) Miller planes.

On the other hand, we successfully obtained crystals with two different shapes using different crystal growth methods. Briefly, NA solid powders were dissolved in ethyl acetate to form a homogenous solution. The solution was then gently drop-cast on the water surface in a Petri dish. The Petri dish was covered and left dark for 48 h, allowing ethyl acetate to evaporate. Long microcrystal rods (300–500 μm in length) were harvested when the organic solvent fully evaporated (Figure 3b and Figure S11). For the plate-like microcrystals, NA solids were first dissolved in *N,N*-dimethylformamide (DMF) to obtain a homogeneous solution ([NA]: 0.25 M). A small amount of the formed solution (50–100 μL) was then rapidly injected into two surfactant aqueous solutions containing sodium dodecyl sulfate with two concentrations ([SDS]: 0.02 M and 0.025 M). One of the aqueous solutions with the higher SDS concentration (0.025 M) was under fierce stirring (\approx 1000 rpm) at 55 °C (labeled as vial 1) to obtain the crystal seeds, and the other one (0.02 M) was kept still to generate a homogenous clear solution (labeled as vial 2) at the same temperature (Figure S12). After 10–15 min of stirring, seed crystals were able to be harvested in vial 1, and about 25 μL suspension solution was gently added into vial 2 for final microcrystal incubation. We harvested rectangular crystalline microplates after 3–5 h (Figure 3c). The microcrystal lengths ranged from 100 to 300 μm, and widths were from 30 to 50 μm (Figure S13).

Powder X-ray diffraction (PXRD) measurements showed that the microrods and microplates were highly crystalline with different preferential crystal facets (Figure 3d). Two prominent peaks at $2\theta = 8.83^\circ$ and 13.29° , respectively, were associated with the (002) and (003) Miller planes when rod crystals lay horizontally on the surface (Figure 3d, orange trace). Except for the (002) and (003) planes, the microplate samples showed another peak

at $2\theta = 16.48^\circ$, corresponding to the $(01\bar{2})$ Miller plane. The (002) and (003) planes were parallel to each other and had an angle of approximately 61° with the $(01\bar{2})$ plane. All three planes were along the crystallographic a -axis (Figure 3e). NA molecules were also expected to stack along this axis as it is the shortest axis that favors the assembled molecules during the crystal growth (Table S1).

The photoresponsive behavior varied in NA crystals that held different shapes. When exposed to UV light, microplate crystals showed cracking and fissures but maintained their overall morphology. Moreover, the crystal plane slightly expanded after light irradiation (Figure 4a–d and Movie S1). In contrast, the microcrystal rods exhibited significant bending under UV light irradiation (Figure 4e,h and Movie S2). The bending was reserved and did not revert to straight. The NA bulk polycrystals, however, splintered and shattered upon the same light irradiation, showing photosolient motions (Figure 4i,j and Movie S3). It was also noticeable that microplates and bulk crystals started to move and deform once the excitation was switched on, whereas the microrods bent with the extended light irradiation duration (Figure 4c,h). All three types of crystals turned amorphous after prolonged light irradiation (Figures S11, S14, and S15). Interestingly, during the light irradiation period, we observed brighter fluorescence from the illuminated samples, suggesting a light-induced fluorescence “turn-on” phenomenon (Figure 4c,g,k). Moreover, the fluorescence emission from the microcrystal plates and rods seemed brighter and closer to white light emission. The fluorescence enhancements would recede as the photocycloaddition progressed, indicating a metastable transition state during the solid-state photochemistry. We inferred that the molecular structural and geometric changes during the $[2 + 2]$ photocycloaddition may have caused high distortion and internal strains of the crystal lattice, enabling macroscopic mechanical deformations. As the molecular orientation varies in crystals with different shapes, the interfacial stress between NA monomer and photodimer molecules would also differ, resulting in disparate mechanical motions. We also observed microrods cracked at the bending locations, similar to the illuminated microplate samples (Figure S16). Because NA molecules primarily orientate along the (002) and (003) Miller planes, the microcrystal rods were expected to show a similar cracking motion as the microplates did upon light irradiation.

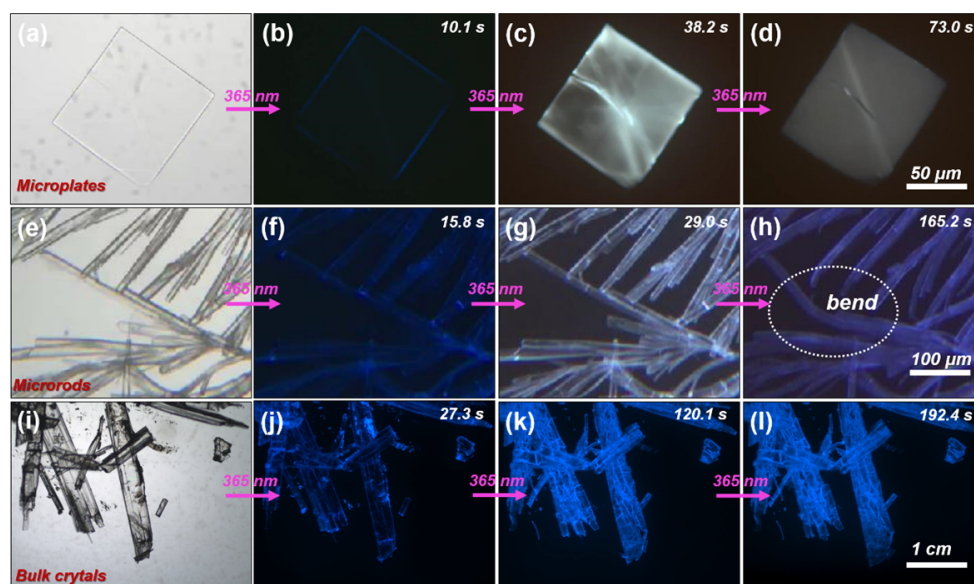


Figure 4. (a–d) Sequential fluorescence microscope images of an NA microcrystal plate showing splintering under light irradiation. (e–h) Sequential fluorescence microscope images of NA microcrystal rods exhibiting bending under light irradiation. (i–l) Sequential fluorescence microscope images of NA bulk polycrystals showing cracking under light irradiation. The excitation light wavelength was 365 nm with an intensity of approximately 20 mW/cm^2 .

Previous literature suggested that the intermolecular couplings were weakened during the [2 + 2] photocycloaddition, enabling an increased fluorescence intensity [9,37,38]. We then measured the steady-state fluorescence spectra of the illuminated NA solids to investigate the intermediate fluorescence emission during the photochemical reaction. We chose the NA polycrystals for measurements to exclude the factor of water and other species like surfactants that would affect the fluorescence. Specifically, NA solid powders were first dissolved in the THF, and the solutions were drop-cast upon the quartz surface to allow solvent evaporation in the dark. We were able to obtain NA polycrystalline thin films formed after 4–6 h. These films were irradiated by UV light for different periods before the fluorescence spectroscopy measurements. NA polycrystals displayed a broad fluorescence emission peak from 400–500 nm (Figure 5a, black trace). After 10 s of light irradiation, the fluorescence emission band exhibited a redshift of approximately 50 nm, and the corresponding intensity slightly declined (Figure 5a, brown trace). However, the fluorescence intensity increased when the irradiation time was 20 s and continued to rise with the prolonged light irradiation period. When the irradiation time was 60 s, the fluorescence intensity reached the highest level, showing more than a factor of 2 compared to the initial samples (Figure 5a, orange trace). However, as the photochemistry proceeded, the fluorescence intensity gradually decreased (Figure 5b). When the irradiation duration was about 1.5 h, the intensity ceased to decline as the photochemistry was accomplished. The final intensity was only about 20% compared to the initial intensity, indicating that the photodimer was less emissive than the NA monomer (Figures 5a,b and S17). Moreover, compared to the ^1H NMR data in Figure 2d, when the light irradiation duration was 60 s, approximately 40% of photodimer molecules were generated there. Therefore, the intermediate fluorescence enhancement was unable to be ascribed to the formation of photodimer molecules. In contrast, dilute solution samples showed much brighter fluorescence and gradually quenched upon the UV light irradiation (Figure 5c). Therefore, we inferred that the enhancement of fluorescence induced by UV light irradiation resulted from alterations in the molecular arrangement, which was intimately related to the ratio of monomers to dimers during the irradiation process. An individual NA molecule is planar and rigid, and the intramolecular conjugation of an NA molecule is also robust due to the C=C bond in vinyl structure, carboxylic acid unit, and naphthalene rings, resulting in a highly emissive nature. The close packing structure of solid crystals hampered effective fluorescence at the beginning. When a photochemical reaction propagates, the intermolecular conjugations between the planar monomer molecules could be destroyed. More photodimer molecules would also favor isolating monomer molecules, facilitating radiation relaxation that enables fluorescence. Our results are also consistent with previous literature [39,40].

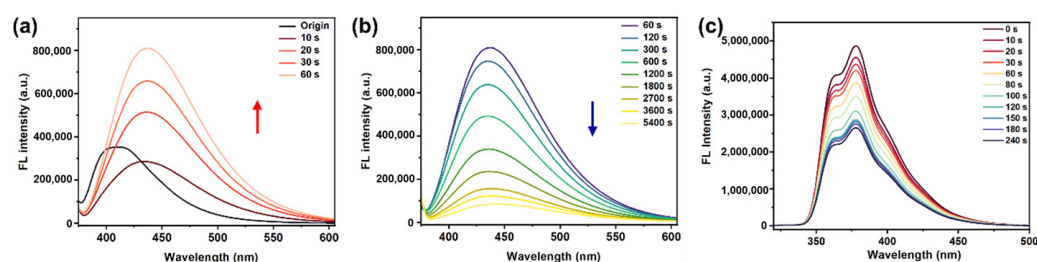


Figure 5. (a,b) The steady-state fluorescence emission spectra of NA demonstrated the variation in fluorescence intensity with different irradiation times for solid powders. Initially, the fluorescence intensity increased and then decreased, accompanied by a maximum red shift of 30 nm ($\lambda_{\text{ex}} = 355$ nm). (c) The steady-state fluorescence emission spectra of NA illustrated the change in fluorescence intensity with different irradiation times in the THF solution. As the irradiation time increased, the fluorescence intensity decreased ($\lambda_{\text{ex}} = 300$ nm).

To get a deeper understanding of the molecular mechanism, we conducted an analysis of the non-covalent interactions (NCIs) between paired monomeric molecules [41–47]. The NCI analysis method provides a visual representation of regions where non-covalent interactions occur in real space, enabling the differentiation between hydrogen bonding, Van der Waals interactions, and steric repulsion. It offers a comprehensive depiction of the types and intensities of non-covalent interactions, thereby effectively aiding research in the field of non-covalent interaction studies. The intermolecular energy was determined to be approximately -8.2 kcal/mol, indicating that robust intermolecular interactions (Figure 6a). The Gibbs free energy (ΔG) is a pivotal parameter in evaluating the potential limits of a chemical reaction. Within the scope of this investigation, we conducted separate geometric optimizations and vibrational frequency analyses for both the monomer and dimeric forms. These calculations determined the Gibbs free energies, denoted as G^θ (NA) for the monomer and G^θ (NA-dimer) for the dimer, respectively. Subsequently, the Gibbs free energy change ($\Delta G^\theta(r)$) associated with the dimerization process was calculated to be 0.029 Kcal/mol, indicative of a positive value (Table S4). This theoretical result is corroborated by experimental data, demonstrating that a significant influx of energy supplied by photoexcitation at a wavelength of 365 nm is essential to initiate the $[2 + 2]$ cycloaddition within the crystalline matrix. Subsequently, molecular orbitals were investigated using density functional theory (DFT) calculations. The three-dimensional frontier molecular orbital scheme reveals that the highest occupied molecular orbitals (HOMOs) predominantly resided on the naphthalene backbone, while the lowest unoccupied molecular orbitals (LUMOs), influenced by electron push-pull effects, displayed off-domain characteristics (Figure 6b). The energy gap between HOMO and LUMO was approximately 3.89 eV, consistent with the observed UV–VIS absorption band at 260 nm. In contrast, the photodimer exhibited a significantly higher energy gap of 4.64 eV, showing itself as more stable (Figure 6b). According to quantum mechanics principles, a greater HOMO–LUMO gap corresponds to a higher energy threshold for electronic transitions within the molecules. This implies a lower possibility of electronic transition, such as light absorption or involvement in charge transfer processes. Additionally, the formation of photodimers involving neighboring NA or NA dimer segments poses challenges. The computational results align with our hypothesis regarding fluorescence switching and the $[2 + 2]$ cycloaddition process in the solid state. It also reveals that NA molecules mainly experience two distinct photophysical pathways when exposed to UV light: non-radiative relaxation through $[2 + 2]$ photocycloaddition and radiative transition leading to activation of isolated monomer fluorescence. Initially, due to the delocalization of the π -dimer, $[2 + 2]$ cycloaddition occurred, yielding a high-energy NA dimer incapable of absorbing energy for photon emission, thus rendering it essentially non-fluorescent upon UV irradiation initiation. Furthermore, the photocycloaddition reduced the intermolecular distance between carbon atoms within the potential reaction double bond. The formation of cyclobutane induced an expansion of both the naphthalene and carboxyl units from their original positions, resembling a butterfly spreading the naphthalene wings. This expansion significantly increased steric hindrance, impeding further photodimer formation and obstructing non-radiative transitions between adjacent monomer molecules. Consequently, it effectively segregated monomers surrounding the dimer and diminished overall crystal fluorescence emission.

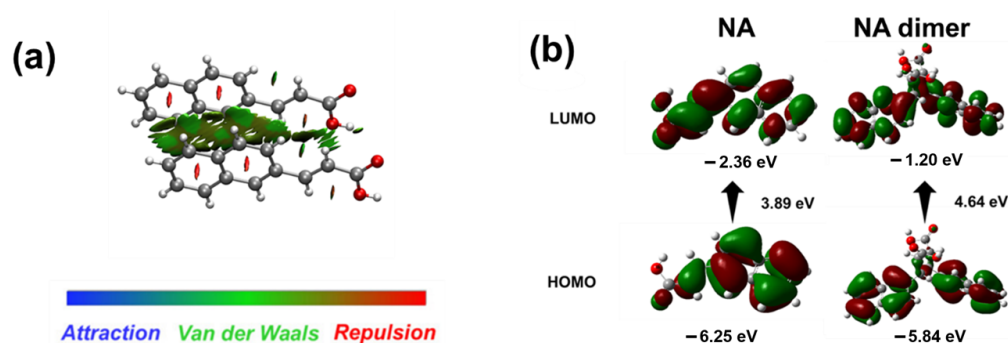


Figure 6. (a) NCI analysis of the intermolecular interactions within excited NA monomer molecules. The scale bar shows the intermolecular interactions between two monomers. (b) Optimized molecular structures and calculated molecular orbital energy levels of the HOMO and LUMO of the NA and photodimer.

The mixture of photoproducts containing monomer and photodimer continues to emit after two days, indicating that the intermediate fluorescence ‘turned-on’ state is relatively stable and can be controlled by the duration of irradiation (Figure S18). The fluorescence-enhancing properties of NA crystals might be effectively utilized in fluorescent information storage applications. Fluorescence encryption might be achieved by precisely controlling the duration of light irradiation based on the stable photoproduct when exposed to UV light. As a proof of concept, we developed a writing-erasing paper incorporating the NA compound (refer to Figure 7). Initially, circular filter paper impregnated with a THF solution of NA monomer was allowed to dry. Subsequently, the letter ‘T’ was inscribed onto the circular filter paper using UV irradiation with a light-proof mask. However, unlike the rest of the circular filter paper, the letter ‘T’ written using the dimer compound did not emit light after one hour of UV light exposure. Conversely, the remaining portion of the filter paper exhibited increasing fluorescence intensity with prolonged light irradiation, thus revealing encrypted information. Following an hour of UV light exposure, there was no longer any illumination in the circular area surrounding the filter paper, indicating the destruction of encrypted information.

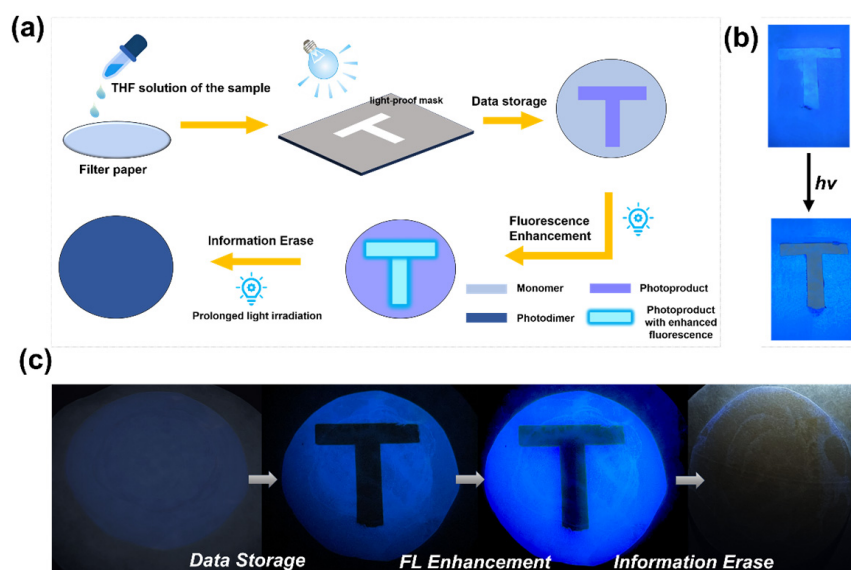


Figure 7. (a) Scheme of the preparation process of NA for information storage. (b) Snapshots showing the fluorescence change of NA on filter paper under light irradiation. (c) Snapshots displaying the information input, fluorescence enhancement, and information erase process on a filter paper based on NA solids.

4. Conclusions

In conclusion, we investigated the photomechanical motions in the molecular crystals composed of a naphthyl derivative, NA. NA crystals with different shapes and sizes, including bulk polycrystals, microcrystal rods, and plates, were successfully prepared using varying crystal growth methods. Crystals exhibited various mechanical motions and deformations driven by the [2 + 2] photocycloaddition, involving disintegration, cracking, bending, and splintering under excitation light irradiation. Simultaneously, an abnormal fluorescence enhancement was observed due to the isolation of monomer molecules during the photochemical reaction. The interesting fluorescence turned-on phenomenon was relatively stable and lasted for days, which can be potentially applied in fabricating light-responsive encryption information systems. Our results demonstrate that crystal morphology and reaction kinetics must be considered when designing a structure with a well-defined photomechanical response. Our results can be an effective platform for adjusting the solid-state properties of naphthyl derivatives and have great potential for practical applications.

Supplementary Materials: The following supporting information can be downloaded at <https://www.mdpi.com/article/10.3390/cryst14060492/s1>. Figure S1. Synthesis of compound NA; Figure S2. ^1H NMR spectrum of NA in Acetone- d_6 ; Figure S3. ^{13}C NMR spectrum of NA in Acetone- d_6 ; Figure S4. The MS spectrum of NA; Figure S5. The MS spectrum of NA-Dimer; Figure S6. UV-Vis absorption spectrum of an NA solid sample mixed with BaSO_4 without light exposure; Figure S7. ^1H NMR spectra of the illuminated solid dimer samples with different wave length light exposure dissolved in the DMSO- d_6 ; Figure S8. ^1H NMR spectra of the illuminated solid samples with heating dissolved in the DMSO- d_6 ; Figure S9. TGA and DSC curves of NA crystals before and after irradiation; Figure S10. Steady-state fluorescence emission spectra of NA in solid state; Figure S11. Optical microscope diagram and cross-polarized microscope image of the initial state and irradiated state of NA microrod crystals; Figure S12. The preparation procedures of NA microplate crystals; Figure S13. The initial state of NA microplate microcrystals is shown in the optical microscope diagram and cross-polarized microscope image; Figure S14. Optical microscope diagram and cross-polarized microscope image of the initial state and irradiated state of NA microplate crystals; Figure S15. Optical microscope diagram and cross-polarized microscope image of the initial state and irradiated state of NA bulk crystals; Figure S16. SEM images of the NA microrod crystal before and after irradiation with 365 nm light; Figure S17. Steady-state fluorescence emission spectra of NA-dimer in solid state; Figure S18. Characterization of the luminescent sustaining properties of NA crystals in solid state; Table S1. Crystal data and structure refinement for NA; Table S2. Table of various conditions for crystal preparation by seed and floating drop methods; Table S3. NCI analysis of the intermolecular interactions; Table S4. The table of Gibbs Free Energy; Table S5. The table of PLQY of NA with different light irradiation time; Movie S1. Microplate crystal under light exposure; Movie S2. Microrod crystal under light exposure; Movie S3. Bulk crystal under light exposure.

Author Contributions: Conceptualization, F.T.; methodology and experiments, T.-Y.L., Y.-Z.D., T.-Y.X. and T.-L.Z.; original draft writing, F.T. and T.-Y.L.; the article was written and revised through the contributions of all authors. All authors have read and agreed to the published version of the manuscript.

Funding: This research was funded by the National Natural Science Foundation of China (NSFC) (grant no. 22105071 and 22375063), the Science and Technology Commission of Shanghai Municipality (grant no. 22ZR1417100 and 23JC1401700), and the Fundamental Research Funds for the Central Universities.

Data Availability Statement: Data is contained within the article or Supplementary Material.

Acknowledgments: We thank the Research Center of Analysis and Test of East China University of Science and Technology for help with the characterization.

Conflicts of Interest: The authors declare no conflicts of interest.

References

1. Yu, Q.; Aguila, B.; Gao, J.; Xu, P.; Chen, Q.; Yan, J.; Xing, D.; Chen, Y.; Cheng, P.; Zhang, Z.; et al. Photomechanical Organic Crystals as Smart Materials for Advanced Applications. *Chem. Eur. J.* **2019**, *25*, 5611–5622. [[CrossRef](#)]
2. Awad, W.M.; Davies, D.W.; Kitagawa, D.; Mahmoud Halabi, J.; Al-Handawi, M.B.; Tahir, I.; Tong, F.; Campillo-Alvarado, G.; Shtukenberg, A.G.; Alkhidir, T.; et al. Mechanical Properties and Peculiarities of Molecular Crystals. *Chem. Soc. Rev.* **2023**, *52*, 3098–3169. [[CrossRef](#)]
3. Kim, T.; Zhu, L.; Al-Kaysi, R.O.; Bardeen, C.J. Organic Photomechanical Materials. *ChemPhysChem* **2014**, *15*, 400–414. [[CrossRef](#)]
4. Seki, T.; Hoshino, N.; Suzuki, Y.; Hayashi, S. Functional Flexible Molecular Crystals: Intrinsic and Mechanoresponsive Properties. *CrystEngComm* **2021**, *23*, 5686–5696. [[CrossRef](#)]
5. Zheng, X.; Liu, X.; Liu, L.; Li, X.; Jiang, S.; Niu, C.; Xie, P.; Liu, G.; Cao, Z.; Ren, Y.; et al. Multi-Stimuli-Induced Mechanical Bending and Reversible Fluorescence Switching in a Single Organic Crystal. *Angew. Chem. Int. Ed.* **2022**, *61*, e202113073. [[CrossRef](#)] [[PubMed](#)]
6. Wang, H.; Xing, H.; Gong, J.; Zhang, H.; Zhang, J.; Wei, P.; Yang, G.; Lam, J.W.Y.; Lu, R.; Tang, B.Z. “Living” Luminogens: Light Driven ACQ-to-AIE Transformation Accompanied with Solid-State Actuation. *Mater. Horiz.* **2020**, *7*, 1566–1572. [[CrossRef](#)]
7. Koshima, H.; Matsuo, R.; Matsudomi, M.; Uemura, Y.; Shiro, M. Light-Driven Bending Crystals of Salicylidenebenzylamines in Enantiomeric and Racemate Forms. *Cryst. Growth Des.* **2013**, *13*, 4330–4337. [[CrossRef](#)]
8. Taniguchi, T.; Fujisawa, J.; Shiro, M.; Koshima, H.; Asahi, T. Mechanical Motion of Chiral Azobenzene Crystals with Twisting upon Photoirradiation. *Chem. Eur. J.* **2016**, *22*, 7950–7958. [[CrossRef](#)] [[PubMed](#)]
9. Sun, J.; Li, W.; Chen, C.; Ren, C.; Pan, D.; Zhang, J. Photoinduced Bending of a Large Single Crystal of a 1,2-Bis(4-pyridyl) ethylene-Based Pyridinium Salt Powered by a [2 + 2] Cycloaddition. *Angew. Chem. Int. Ed.* **2013**, *125*, 6785–6789. [[CrossRef](#)]
10. Zhu, L.; Tong, F.; Zaghoul, N.; Baz, O.; Bardeen, C.J.; Al-Kaysi, R.O. Characterization of a P-Type Photomechanical Molecular Crystal Based on the E → Z Photoisomerization of 9-Divinylanthracene Malonitrile. *J. Mater. Chem. C* **2016**, *4*, 8245–8252. [[CrossRef](#)]
11. Zhu, L.; Al-Kaysi, R.O.; Bardeen, C.J. Reversible Photoinduced Twisting of Molecular Crystal Microribbons. *J. Am. Chem. Soc.* **2011**, *133*, 12569–12575. [[CrossRef](#)] [[PubMed](#)]
12. Saha, S.; Desiraju, G.R. Crystal Engineering of Hand-Twisted Helical Crystals. *J. Am. Chem. Soc.* **2017**, *139*, 1975–1983. [[CrossRef](#)]
13. Kitagawa, D.; Nishi, H.; Kobatake, S. Photoinduced Twisting of a Photochromic Diarylethene Crystal. *Angew. Chem. Int. Ed.* **2013**, *52*, 9320–9322. [[CrossRef](#)]
14. Kim, T.; Zhu, L.; Mueller, L.J.; Bardeen, C.J. Mechanism of Photoinduced Bending and Twisting in Crystalline Microneedles and Microribbons Composed of 9-Methylanthracene. *J. Am. Chem. Soc.* **2014**, *136*, 6617–6625. [[CrossRef](#)]
15. Bartholomew, A.K.; Stone, I.B.; Steigerwald, M.L.; Lambert, T.H.; Roy, X. Highly Twisted Azobenzene Ligand Causes Crystals to Continuously Roll in Sunlight. *J. Am. Chem. Soc.* **2022**, *144*, 16773–16777. [[CrossRef](#)]
16. Shu, Y.; Ye, K.; Sun, J.; Yue, Y.; Liu, C.; Wang, H.; Lu, R. Thermo-Induced Single-Crystal-to-Single-Crystal Transformations and Photo-Induced [2 + 2] Cycloaddition Reactions in Polymorphs of Chalcone-Based Molecular Crystals: Multi-Stimuli Responsive Actuators. *Chem. Eur. J.* **2021**, *27*, 17960–17969. [[CrossRef](#)]
17. Kim, T.; Al-Muhanna, M.K.; Al-Suwaidan, S.D.; Al-Kaysi, R.O.; Bardeen, C.J. Photoinduced Curling of Organic Molecular Crystal Nanowires. *Angew. Chem. Int. Ed.* **2013**, *52*, 6889–6893. [[CrossRef](#)]
18. Ye, Y.; Gao, L.; Hao, H.; Yin, Q.; Xie, C. Tuning the Photomechanical Behavior and Excellent Elasticity of Azobenzene via Cocrystal Engineering. *CrystEngComm* **2020**, *22*, 8045–8053. [[CrossRef](#)]
19. Wang, H.; Chen, P.; Wu, Z.; Zhao, J.; Sun, J.; Lu, R. Bending, Curling, Rolling, and Salient Behavior of Molecular Crystals Driven by [2 + 2] Cycloaddition of a Styrylbenzoxazole Derivative. *Angew. Chem. Int. Ed.* **2017**, *56*, 9463–9467. [[CrossRef](#)]
20. Al-Kaysi, R.O.; Müller, A.M.; Bardeen, C.J. Photochemically Driven Shape Changes of Crystalline Organic Nanorods. *J. Am. Chem. Soc.* **2006**, *128*, 15938–15939. [[CrossRef](#)]
21. Chalek, K.R. Bridging Photochemistry and Photomechanics with NMR Crystallography: The Molecular Basis for the Macroscopic Expansion of an Anthracene Ester Nanorod. *Chem. Sci.* **2021**, *12*, 453–463. [[CrossRef](#)] [[PubMed](#)]
22. Kobatake, S.; Takami, S.; Muto, H.; Ishikawa, T.; Irie, M. Rapid and Reversible Shape Changes of Molecular Crystals on Photoirradiation. *Nature* **2007**, *446*, 778–781. [[CrossRef](#)] [[PubMed](#)]
23. Xu, T.-Y.; Tong, F.; Xu, H.; Wang, M.-Q.; Tian, H.; Qu, D.-H. Engineering Photomechanical Molecular Crystals to Achieve Extraordinary Expansion Based on Solid-State [2 + 2] Photocycloaddition. *J. Am. Chem. Soc.* **2022**, *144*, 6278–6290. [[CrossRef](#)] [[PubMed](#)]
24. Koshima, H.; Taniguchi, T.; Asahi, T. Mechanically Responsive Crystals by Light and Heat. In *Mechanically Responsive Materials for Soft Robotics*; Koshima, H., Ed.; Wiley: Hoboken, NJ, USA, 2020; pp. 57–82. [[CrossRef](#)]
25. Zhang, Q.; Qu, D.; Tian, H. Photo-Regulated Supramolecular Polymers: Shining Beyond Disassembly and Reassembly. *Adv. Opt. Mater.* **2019**, *7*, 1900033. [[CrossRef](#)]
26. Shih, B.; Shah, D.; Li, J.; Thuruthel, T.G.; Park, Y.-L.; Iida, F.; Bao, Z.; Kramer-Bottiglio, R.; Tolley, M.T. Electronic Skins and Machine Learning for Intelligent Soft Robots. *Sci. Robot.* **2020**, *5*, eaaz9239. [[CrossRef](#)] [[PubMed](#)]
27. Borré, E.; Stumbé, J.; Bellemin-Laponnaz, S.; Mauro, M. Light-Powered Self-Healable Metallosupramolecular Soft Actuators. *Angew. Chem. Int. Ed.* **2016**, *128*, 1335–1339. [[CrossRef](#)]

28. Al-Kaysi, R.; Tong, F.; Al-Haidar, M.; Zhu, L.; Bardeen, C.J. Highly Branched Photomechanical Crystals. *Chem. Commun.* **2017**, *53*, 2622–2625. [[CrossRef](#)] [[PubMed](#)]
29. Peng, J.; Zhao, J.; Ye, K.; Gao, H.; Sun, J.; Lu, R. Light-Induced Bending of Needle-Like Crystals of Naphthylvinylbenzoxazole Triggered by Trans—Cis Isomerization. *Chem.-Asian J.* **2018**, *13*, 1719–1724. [[CrossRef](#)] [[PubMed](#)]
30. Yu, Q.; Yang, X.; Chen, Y.; Yu, K.; Gao, J.; Liu, Z.; Cheng, P.; Zhang, Z.; Aguila, B.; Ma, S. Fabrication of Light-Triggered Soft Artificial Muscles via a Mixed-Matrix Membrane Strategy. *Angew. Chem. Int. Ed.* **2018**, *57*, 10192–10196. [[CrossRef](#)] [[PubMed](#)]
31. Bhandary, S.; Beliš, M.; Bourda, L.; Kaczmarek, A.M.; Van Hecke, K. Visible Light-fueled Mechanical Motions with Dynamic Phosphorescence Induced by Topochemical [2 + 2] Reactions in Organoboron Crystals. *Angew. Chem. Int. Ed.* **2023**, *62*, e202304722. [[CrossRef](#)]
32. Eslami, H.; Müller-Plathe, F. Self-Assembly Pathways of Triblock Janus Particles into 3D Open Lattices. *Small* **2024**, *20*, 2306337. [[CrossRef](#)]
33. Tong, F.; Hanson, M.P.; Bardeen, C.J. Analysis of Reaction Kinetics in the Photomechanical Molecular Crystal 9-Methylantracene Using an Extended Finke–Watzky Model. *ChemPhysChem* **2016**, *18*, 31936–31945. [[CrossRef](#)]
34. Tong, F.; Xu, W.; Al-Haidar, M.; Kitagawa, D.; Al-Kaysi, R.O.; Bardeen, C.J. Photomechanically Induced Magnetic Field Response by Controlling Molecular Orientation in 9-Methylantracene Microcrystals. *Angew. Chem. Int. Ed.* **2018**, *57*, 7080–7084. [[CrossRef](#)] [[PubMed](#)]
35. Morimoto, K.; Kitagawa, D.; Tong, F.; Chalek, K.; Mueller, L.J.; Bardeen, C.J.; Kobatake, S. Correlating Reaction Dynamics and Size Change during the Photomechanical Transformation of 9-Methylantracene Single Crystals. *Angew. Chem. Int. Ed.* **2022**, *134*, e202114089. [[CrossRef](#)]
36. Ogawa, K.; Harada, J.; Fujiwara, T.; Takahashi, H. UV-vis Absorption Spectra of Powdered Materials: Direct Measurements by Optical Waveguide Spectroscopy. *Chem. Lett.* **2004**, *33*, 1446–1447. [[CrossRef](#)]
37. Yue, Y.; Dai, J.; Jin, L.; Liu, C.; Sun, J.; Ye, K.; Lu, R. The Factor beyond Schmidt’s Criteria Impacting the Photo-Induced [2 + 2] Cycloaddition Reactivity and Photoactuation of Molecular Crystals Based on Cyclic Chalcone Analogues. *Chem. Eur. J.* **2023**, *29*, e202301525. [[CrossRef](#)]
38. Pan, G.; Wu, Z.; Liu, Z.; Xu, B.; Tian, W. Photoinduced Fluorescence Switching in Molecular Aggregates by Topological [2 + 2] Cycloaddition. *Angew. Chem. Int. Ed.* **2023**, *62*, e202303152. [[CrossRef](#)] [[PubMed](#)]
39. Schmidt, G.M.J. Photodimerization in the Solid State. *Pure Appl. Chem.* **1971**, *27*, 647–678. [[CrossRef](#)]
40. Johnson, E.R.; Keinan, S.; Mori-Sánchez, P.; Contreras-García, J.; Cohen, A.J.; Yang, W. Revealing Noncovalent Interactions. *J. Am. Chem. Soc.* **2010**, *132*, 6498–6506. [[CrossRef](#)] [[PubMed](#)]
41. Boys, S.F.; Bernardi, F. The Calculation of Small Molecular Interactions by the Differences of Separate Total Energies. Some Procedures with Reduced Errors. *Mol. Phys.* **1970**, *19*, 553–566. [[CrossRef](#)]
42. Humphrey, W.; Dalke, A.; Schulten, K. VMD: Visual Molecular Dynamics. *J. Mol. Graph.* **1996**, *14*, 33–38. [[CrossRef](#)] [[PubMed](#)]
43. Lu, T.; Chen, F. Multiwfn: A Multifunctional Wavefunction Analyzer. *J. Comput. Chem.* **2012**, *33*, 580–592. [[CrossRef](#)] [[PubMed](#)]
44. Alves Machado Filho, M.; Hsiao, C.-L.; Dos Santos, R.B.; Hultman, L.; Birch, J.; Gueorguiev, G.K. Self-Induced Core–Shell InAlN Nanorods: Formation and Stability Unraveled by Ab Initio Simulations. *ACS Nanosci. Au* **2023**, *3*, 84–93. [[CrossRef](#)] [[PubMed](#)]
45. Chen, J.; Li, S.; Wang, X.; Fang, L.; Huang, D.; Ke, L.; Chen, J.; Wang, Q.; Zhang, H.; Wu, Y.; et al. Synthesis and Characterization of Pressure-Sensitive Adhesives Based on a Naphthyl Curing Agent. *Polymers* **2023**, *15*, 4516. [[CrossRef](#)] [[PubMed](#)]
46. Akkarasamiyo, S.; Margalef, J.; Samec, J.S.M. Nickel-Catalyzed Suzuki–Miyaura Cross-Coupling Reaction of Naphthyl and Quinolyl Alcohols with Boronic Acids. *Org. Lett.* **2019**, *21*, 4782–4787. [[CrossRef](#)]
47. Singh, R.B.; Mahanta, S.; Bagchi, A.; Guchhait, N. Interaction of Human Serum Albumin with Charge Transfer Probeethyl Ester of N,N-Dimethylamino Naphthyl Acrylic Acid: An Extrinsic Fluorescence Probe for Studying Protein Micro-Environment. *Photochem. Photobiol. Sci.* **2009**, *8*, 101–110. [[CrossRef](#)]

Disclaimer/Publisher’s Note: The statements, opinions and data contained in all publications are solely those of the individual author(s) and contributor(s) and not of MDPI and/or the editor(s). MDPI and/or the editor(s) disclaim responsibility for any injury to people or property resulting from any ideas, methods, instructions or products referred to in the content.